Photodetectors Based on Heterostructures for Opto-Electronic Applications

Bahram Nabet, *Member, IEEE*, Adriano Cola, Andrea Cataldo, Xiying Chen, and Fabio Quaranta

***Abstract*—In this paper, we present four photodetector devices that have the benefit of compatibility with established high electron-mobility transistor technology and are, thus, more conducive to monolithic integration with high-speed opto-electronic integrated circuitry. These AlGaAs–GaAs heterojunction-based planar devices all use the wide-gap material to enhance the Schottky barrier height between metal and semiconductor. We show that doping of this layer produces an internal electric field that aids in the transport and collection of photoelectrons. Addition of a resonant optical cavity by means of a distributed Bragg reflector reduces the required thickness of the absorption layer, thus achieving good responsivity and high speed, as well as wavelength selectivity. Current–voltage, current–temperature, photocurrent spectra, high-speed time response, and on-wafer frequency-domain measurements are presented, which point out that the often contradictory requirements of responsivity, noise, and speed may be addressed by proper engineering of the internal electric field and optical properties. Numerical simulations are performed to describe internal electric and optical behavior and a small-signal model based on frequency-domain data is extracted in order to facilitate photoreceiver design. The low dark current, in tens of femtoamps per square micrometer, full-width at half-maximum time responses below 10 ps, and high bandwidth in tens of gigahertz, make these devices of interest for applications ranging from optical communications to imaging systems.**

***Index Terms*—Distribute Bragg reflector, heterojunction, heterostructure metal–semiconductor–metal (MSM), high electron mobility, photodetector, resonant cavity enhanced (RCE), Schottky contact, two-dimensional electron gas (2-DEG).**

I. Introduction

THE development of high-speed photodetector technologies that are more conducive to monolithic integration with high-speed circuitry is critical to the realization of practical opto-electronic integrated circuitry (OEIC). In current fiber-optic lightwave communications systems, the front-end receiver plays a crucial role, having to satisfy stringent requirements on speed, noise characteristics, and responsivity [1], [2]. Since these opto-electronic receivers are realized by monolithic integration of photodetectors and transistor amplifier circuits, compatibility of the device structure and technology with the transistor becomes increasingly important [3]–[8]. The trend toward monolithic OEIC motivates appreciable research activity directed toward the employment of planar photodetectors, which can be easily fabricated and are compatible with the field-effect transistor (FET) process [1], [3], in the same manner that p-i-n detectors and bipolar transistor technology become natural counterparts [9], [10]. This integration allows for optimization of circuit components including detectors, transistors, and the requisite matching circuitry. On the other hand, the primary feature for a good receiver is the high-frequency performance, hence, techniques that would relieve the burden of gain-bandwidth product limitation become relevant.

The demand for gigabit-speed fiber-optic communication and the popularity of fiber optics in RF/microwave systems has led to many advances in high-speed photodetector technology. Specific application requirements have spurred development of novel device structures to improve the speed, responsivity, and noise performance. This paper discusses two sets of high-speed low-noise photodetectors at near-infrared wavelength, both based on AlGaAs–GaAs heterojunctions that increase the Schottky barrier between metal contacts and the absorption GaAs layer. First, we describe a device in which modulation doping of the wide-gap side of the heterojunction produces an internal field in the absorption region that aids in the transport and collection of optically generated carriers. Second, in order to improve on the speed of response by reducing transit length of the carriers, a resonant cavity is formed by adding a distributed Bragg reflector (DBR) to a properly chosen absorption layer thickness resulting in a resonant cavity enhanced (RCE) photodetector. Delta doping of the wide-gap barrier enhancement layer in this device is also shown to produce an internal electric field, which enhances device performance and can provide high quantum efficiency and high speed, as well as wavelength selectivity.

Similar to a high electron-mobility transistor (HEMT), doping of an AlGaAs–GaAs heterostructure produces a two-dimensional electron gas (2-DEG) at the heterointerface on the narrow-gap side. This 2-DEG is confined in a triangular potential well that is formed on one side due to conduction band discontinuity and on the other side due to band banding, i.e., an internal electric field is formed due to charge transfer across the heterointerface that confines the resultant transferred charge. While in the HEMT device the 2-DEG is contacted by the ohmic source and drain metal through a deep annealing process, in the devices presented here, two Schottky contacts

Manuscript received October 18, 2002; revised May 6, 2003. This work was supported in part by the National Science Foundation under Grant ECS 0117073, by Photonics Laboratories Inc. under a Ballistic Missile Defense Organization Award, and by the Fondo Integrativo Speciale Ricerca under the Few Photons Optical Nanodevices Program.

B. Nabet is with the Electrical and Computer Engineering Department, Drexel University, Philadelphia, PA 19104 USA (e-mail: nabet@cbis.ece.drexel.edu).

A. Cola and F. Quaranta are with New Materials for Electronics, Consiglio Nazionale delle Ricerche, 73100 Lecce, Italy (e-mail: adriano.cola@imm.cnr.it).

A. Cataldo is with the Innovation Engineering Department, University of Lecce, 73100 Lecce, Italy (e-mail: andrea.cataldo@unile.it).

X. Chen was with the Electrical and Computer Engineering Department, Drexel University, Philadelphia, PA 19104 USA. She is now with the Mosel Vitelic Corporation, San Jose, CA 95134 USA.

Digital Object Identifier 10.1109/TMTT.2003.817463

are made on top of the AlGaAs layer. Thus, these are a variation of metal–semiconductor–metal (MSM) photodetector devices where current transport under dark is primarily determined by thermionic emission of carriers across the metal–wide-gap semiconductor. The existence of the 2-DEG, however, is shown to affect this transport of charge partially because of the reduced dimensional nature of the density of states in the semiconductor and partially due to the Coulombic force that this cloud of charge exerts on the emitted carriers from metal [12]. The effect of this force appears as an increase in barrier height and, hence, decreases the thermionic emission current, resulting in a modification to the classic thermionic emission current equation [13] that includes the amount of barrier enhancement due to this electron–electron cloud effect $\Delta\phi_{e-e}$ [12] as follows:

$$I_{3D} = A_{\text{eff}} A^* T^2 \exp\left(-\frac{q\phi_B}{kT}\right) \exp\left(\frac{\Delta\phi_{im}}{kT}\right) \exp\left(-\frac{\Delta\phi_{e-e}}{kT}\right) \text{A}. \tag{1}$$

Here, A_{eff} is the effective contact area, A^* is the Richardson constant, ϕ_{B} is the barrier height between metal and (wide-gap) the semiconductor, and $\Delta\phi_{im}$ is the amount of the barrier lowering by the image force.

Equation (1) suggests that the 2-DEG density control can modify the barrier height and, hence, dark current through the term $\Delta\phi_{e-e}$; we will present experimental results that compare identical structures whose only difference is the doping of the wide-gap material, hence, 2-DEG density, showing exponential reduction in the dark current. The reduction of this dark current is a generic requirement of all photodetector devices since it is inversely proportional to the signal-to-noise ratio. The detector shot noise, which dominates noise of high-speed photodetectors, is also directly related to the dark current [13], thus, its reduction will directly affect device sensitivity. A related main point of this paper is to show that this reduction of dark current does not adversely affect generation, transport, and collection of charge carriers [14], rather, the electric field produced in the vertical direction due to modulation doping facilitates transport of optically generated electrons, thus improving speed and photoresponsivity.

A common problem with planar, as well as vertical, photodetectors is that in order to achieve a fast optical response, the depleted absorption region needs to be small for reduced path length, but this results in decrease of responsivity due to small absorption depth. The resonant cavity technique offers the possibility to balance such a conflict between fast speed and sensitivity [15]. We present RCE heterojunction MSM (RCE–HMSM) devices, which combine the electronic advantages of the built-in field with photonic confinement caused by the resonance cavity, thus overcoming canonical quantum efficiency-bandwidth product limitation, which typically apply to structures in which a depleted absorption layer leads to tradeoffs between quantum efficiency, carrier drift transit time, and *RC* time constant.

In the following, we report on a comprehensive study of the static and dynamic electrical behavior of four devices, which differ in modulation doping and presence of optical cavity. Current–voltage measurements as a function of temperature, capacitance–voltage measurements, and photocurrent spectra are presented under dc bias conditions that show the effect of modulation doping, as well as resonance cavity, on device behavior. High-speed time-response measurements are given, indicating that higher peak amplitude of the transient response is achieved in the presence of higher 2-DEG density without degradation of a temporal response. Simulation is performed in order to gain insight in electronic behavior, and describe optical properties. Microwave measurements taken in the frequency domain complete the picture of characterizations, allowing us to extract the elements of the equivalent circuit required for impedance matching to amplifiers for photoreceiver design.

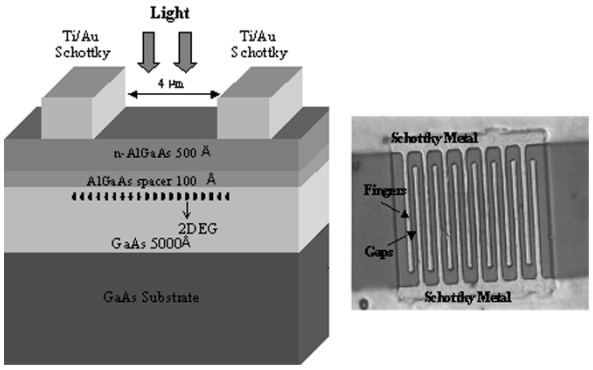

Fig. 1. (*left*) Heterojunction MSM device structure. (*right*) SEM top view of the device showing a planar interdigitated structure.

II. Device Design and Structure

A. HMSM Structure

The device growth structure of the HMSM is that of an enhancement-mode HEMT; on a buffer layer grown on SI–GaAs, 5000 Å of undoped GaAs is deposited followed by 100 Å of an undoped spacer layer of $\text{A1}_{0.24}\text{Ga}_{0.76}\text{As}$ and 500 Å of n-doped $\text{A1}_{0.24}\text{Ga}_{0.76}\text{As}$. A low Al mole fraction is chosen so as to ensure a smooth heterointerface and reduce the so-called DX defect centers that are known to arise for mole fractions above 35%. The two $\text{A1}_{0.24}\text{Ga}_{0.76}\text{As}$ doping levels used in this study, in order to identify the effect of the internal aiding field that results from doping of the wide-gap material, are $\text{N}_d = 3 \times 10^{17}$ cm^{-3} (hereafter called low doping) and 6×10^{17} cm^{-3} (high doping). These values were determined based on both numerical simulations and self-consistent solution of Poisson and Schrödinger equations so as to ensure transfer of charge to GaAs, hence, creation of a triangular quantum well with its associated vertical electric field at that interface. Two Schottky contacts of 600-Å–thickness Ti/Au are deposited on top of the wide-gap material in an interdigital pattern typically used for photodetectors. Fig. 1 shows the schematic of the device structure with a top scanning electron microscopy (SEM) view of a fabricated interdigital photodetector. The device active area is 40 μm $\times$ 40 μm and a matrix of devices with metal fingers of 1- and 2-μm wide and spacing between fingers of 1, 2, and 4 μm were used. Since both contacts are rectifying and symmetric, application of voltage reverse biases one junction and slightly forward biases the other. The reverse-biased junction determines current flow, while the other mainly affects electron collection.

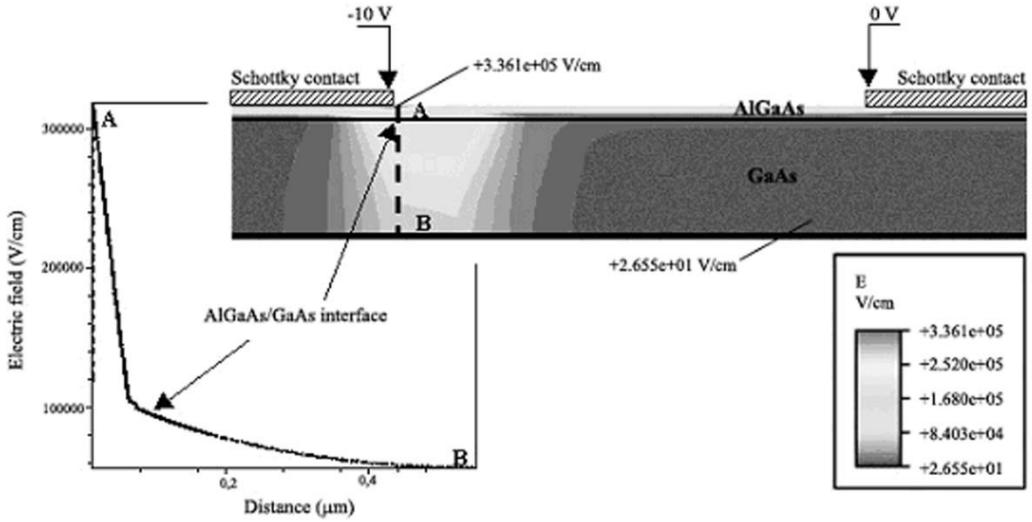

Fig. 2. Two-dimensional simulation of the electric-field distribution and a one-dimensional vertical cut under cathode for an HMSM device: applied bias is 10 V.

The barrier between metal and AlGaAs thus controls current flow through the process of thermionic emission. This configuration is useful in the study of photodetectors that employ barrier enhancement layers for reduction of dark current [16]. It should be repeated that an obvious advantage of this structure is the monolithic integrability of the photodetectors and transistors in both growth and processing that make it suitable for integrated optical detection applications [17].

B. HMSM Simulation

The structure of Fig. 1 has been analyzed by the commercial software package *ISE-TCAD* in order to simulate internal electric field and potential, mobile carrier concentration, and carrier-flow directions. In Fig. 2, the two-dimensional electric-field distribution in a low doping device is plotted along with a one-dimensional cut in the direction of growth. A strong electric field in the thin AlGaAs layer is observed, which, when combined with other simulation results, confirms that this fully depleted layer does not contribute to the dark current. Moreover, due to its energy gap value, this layer is transparent to a radiation of wavelength greater than 720 nm. Thus, the GaAs layer is responsible for both absorption of light and current flow. In GaAs, under the cathode electrode, the peak value of the electric field is approximately 100 kV/cm. The field strongly decreases in the direction along the grounded electrode. This vertical component of the electric field depends on the doping of the AlGaAs layer in the sense that it increases and it penetrates further into GaAs as the AlGaAs doping increases. This is the aiding field, which pushes the photogenerated electrons toward the AlGaAs/GaAs interface. The electrons drift toward the anode by the applied horizontal field and may be partially transported through the triangular well. By the same token, the holes are pushed away from the interface, but once they reach below the cathode, band bending due to cathode Schottky contact facilitates their collection.

C. RCE–HMSM Structure

A typical RCE photodetector is made of a Fabry–Perot cavity, with a mirror on each end, whose length determines the resonant frequency. In practice, the bottom mirror consists of quarter-wave stacks of two different suitable materials forming a DBR. The top mirror can be the interface between the native semiconductor and air due to their large difference of refractive index; here, we use a heterojunction, similar to the structure of the HMSM shown in Fig. 1, to achieve better photon reflection, as well as other important electronic functionalities. Recirculation of photons from the top of this layer and the bottom DBR allows a thin absorption layer L_2 to be used to minimize the response time without hampering the quantum efficiency. Here, quantum efficiency (η) is defined as the ratio of absorbed to incident photons, which can be written as [15]

$$\eta = \frac{(1-R_1)\left(1-e^{-\alpha L_2}\right)\left(1+R_2 e^{-\alpha L_2}\right)}{\left[1-2\sqrt{(R_1R_2)}e^{-\alpha L_2}\cos(2\beta L+\Psi_1+\Psi_2)+R_1R_2e^{-2\alpha L_2}\right]} \tag{2}$$

where L_1 is the nonabsorbing barrier enhancement layer, $\beta L = \beta_1 L_1 + \beta_2 L_2$, R_1, and R_2 are the top and bottom mirror reflectivities, respectively, α is the absorption coefficient of the absorption layer, Ψ_1 and Ψ_2 are phase shifts introduced by top and bottom mirrors, and β_1 and β_2 are the propagation constants in these two materials. From (2), quantum efficiency is maximized when reflection from the DBR is high and the condition $\cos(2\beta L + \Psi_1 + \Psi_2) = 1$ is satisfied.

There are three requirements for the materials to be selected to construct the bottom minor, i.e., large refractive index difference, lattice matching to GaAs substrates, and bandgap larger than that of the active layer so that photons are not absorbed in this layer. Based on their natural material properties, $A1_{0.24}Ga_{0.76}As$ and $A1_{0.9}Ga_{0.1}As$ are suitable pairs to construct this DBR mirror [18]. The top mirror should reduce reflection from air and recirculate the photons reflected from the bottom mirror. A 55-nm layer of $A1_{0.24}Ga_{0.76}As$ has been employed for this purpose, which also offers the following electronic properties. First, this layer lattice matches to the absorption layer, with reduced DX center defect levels due to a low Al mole fraction, while providing surface stability. Second, it enhances the Schottky barrier between metal and GaAs due to its larger bandgap. Third, this layer is delta doped to produce

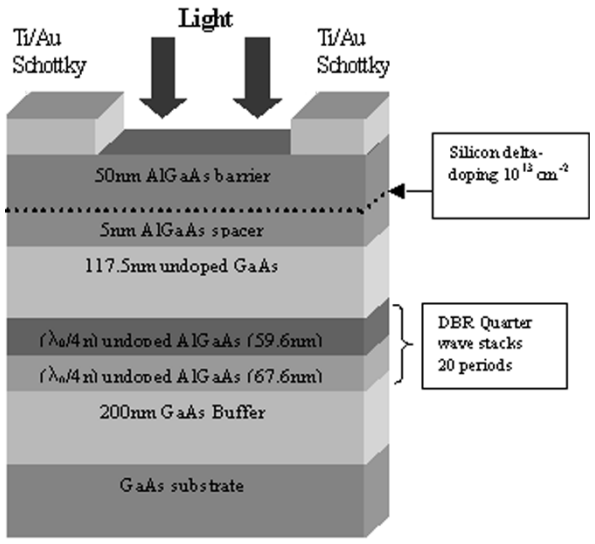

Fig. 3. Device structure of the delta-doped RCE HMSM photodetector.

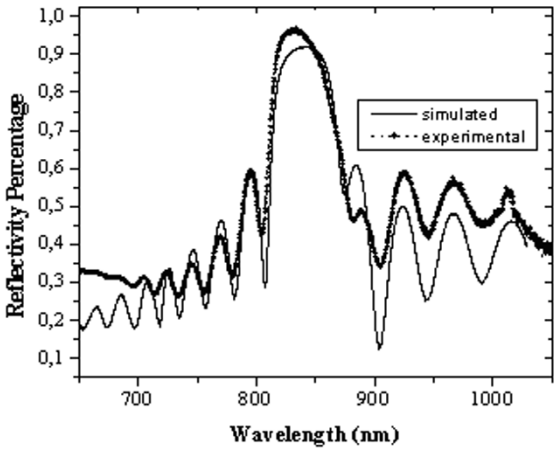

Fig. 4. Comparison of the reflectivity spectrum between experimental data (solid line) and simulation results (dashed line) for the delta-doped RCE–HMSM photodetector.

a 2-DEG that is confined to the vicinity of the heterojunction. The last is the most important novel feature of this device. This top AlGaAs layer is delta doped, rather than uniformly, in order to take advantage of high channel electron density, reduced trapping effects, and improved threshold voltage, as well as high breakdown characteristics.

A schematic cross section of the grown RCE–HMSM is shown in Fig. 3. The layer structure was grown by solid-source molecular beam epitaxy on a semi-insulating GaAs substrate. Twenty periods of $A1_{0.24}Ga_{0.76}As/A1_{0.9}Ga_{0.1}As$ DBR were grown on a 200-nm GaAs buffer layer. The bottom mirror was designed for high reflectance at a 850-nm center wavelength. Absorption layer thickness was 117.5 nm, calculated from the resonance criteria of (2). The thickness of the top barrier enhancement layer was 50 nm and the spacer layer was 5 nm. Silicon was used as the n-type delta-doping layer with a sheet density of 5×10^{12} cm^{-2}, which was grown between barrier enhancement and spacer layers. The device area was 40 μm $\times$ 40 μm with a typical interdigital pattern with finger width (W) of 1 or 2 μm and distance (G) of 2 or 4 μm. For comparison, a device having the same structure, but without silicon delta doping, was also fabricated.

We performed reflectivity measurements as a function of wavelength in order to verify the optical spectral response of the designed structure. The reflectivity measurements are compared to the simulation results in Fig. 4 demonstrating that the typical optical band is exactly centered around the projected wavelength with a full-width at half-maximum (FWHM) of around 60 nm. The differences between the experimental data and simulation results are due to the incident light direction and to optical properties of the actual growth structure. Particularly, in the simulation, the incident light was assumed to be exactly normal to the device, while in testing, there was probably a small variation in this angle. In addition, the heterointerface growth quality affects the shape of the curve, especially near the resonant wavelength. In fact, TEM images takes from the Bragg layers showed a trapezoidal profile that was incorporated in the model of reflectivity resulting in Fig. 4 [20].

D. RCE–HMSM Simulation

Energy bands, charge, electric field, and potential distributions in the delta doped RCE–HMSM structure were analyzed using the *ISE-TCAD* device simulator. One-dimensional self-consistent solution of Poisson and Schrödinger equations were used to verify accuracy of the results in equilibrium.

Comparison between doped and undoped structures showed a great difference in the distribution of the electric field and, particularly, the extent and direction of depletion regions. As shown in Fig. 5 and quantified by a one-dimensional cut in the vertical direction, the applied bias produces a depletion region in the vicinity of the cathode within which the electric field varies sharply in the vertical direction. The triangular well, and associated with it the 2-DEG, extend from the end of this depletion region to the anode. The electric-field flow vectors show strongly vertical orientation compared to the undoped device, which is mostly horizontally oriented. This again indicates strong force exerted on the optically generated electrons toward the top heterointerface, i.e., the 2-DEG, the quantum well and, hence, the anode. Again, holes are pushed toward the bottom of the device, but are now confined to the short thickness of the resonant cavity. Furthermore, the depletion region underneath the cathode has a very high electric field, approximately 300 kV/cm from Fig. 5, which facilitates hole collection. Hence, doping of the wide-gap material results in modification of the band structure, presence of the internal electric field, and a cloud of mobile charge, which significantly change the transport and collection of optically generated carriers.

III. Static Characterization

A. HMSM Static Characterization

Current–voltage characteristics under dark were measured at different temperatures for HMSM devices with uniform doping levels of the AlGaAs layer. The curves reported in Fig. 6 refer to the sample with low AlGaAs doping. The sample with high doping shows a similar behavior, but the activation energy, which is calculated from the slope of the $\ln(I)$ versus $1/kT$ plot, is seen to be higher. These values at 5 V are 0.658 and

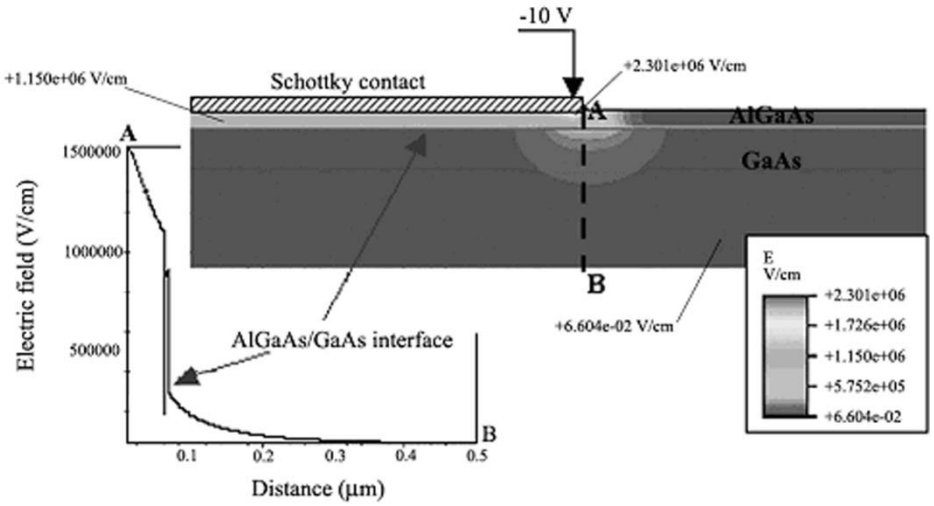

Fig. 5. Two-dimensional simulation of the electric-field distribution and one-dimensional vertical cut under Schottky biased contact for the delta-doped heterojunction: applied bias is 10 V.

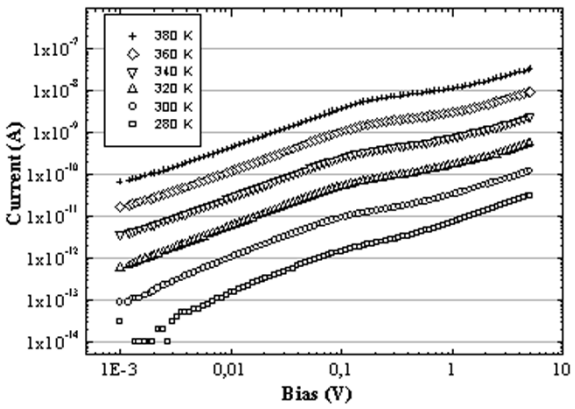

Fig. 6. *I–V* curves under dark at different temperatures for the HMSM low-doping-level device.

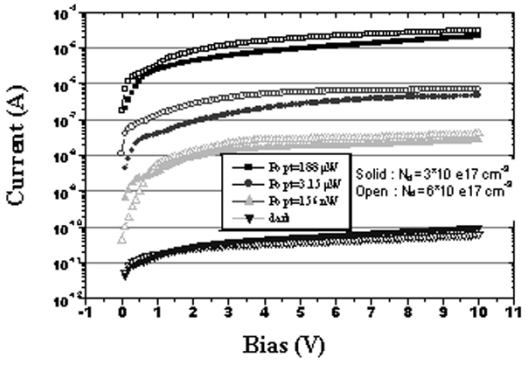

Fig. 7. *I–V* measurements under dark and illumination for the HMSM devices with two different uniform doping levels.

0.677 eV for the low- and high-doping samples, respectively. The difference is in agreement with a proposed model of (1) based on the repulsion between the electron cloud that is formed in the narrow-gap material and the electrons in the metal contact [12].

The *I–V* curves for two different doping levels of the AlGaAs are compared in Fig. 7 in dark and under a 670-nm laser illumination. We observe dark current levels in tens of picoamps, a large dynamic range due to very low noise levels, i.e., more than five order of magnitude change that is observed for approximately 0.2 mW of optical power, as well as lower dark current and larger photoresponse for a higher doping level of AlGaAs.

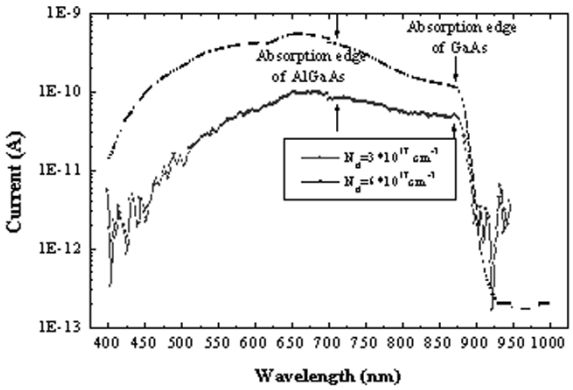

Fig. 8. Photocurrent spectra for the HMSM devices with two different uniform doping levels.

The spectral response of the low- and high-doping samples, in the range of 400–1000 nm, is shown in Fig. 8. A monochrometer with 0.15-nm resolution was used to select the excitation wavelength from a chopped tungsten light source. The signal was measured by a lock-in amplifier and the spectral response was measured under 10-V reverse bias. It is interesting to note that, in the region where only GaAs absorbs, as the wavelength decreases, the high-doping sample increases the collection of photogenerated carriers with respect to the low doping. This result, in conjunction with the data of Fig. 7, is consistent with the aiding role of the vertical electric field, which is stronger in the case of higher doping. We should note that noise observed in the region above the fundamental edge of absorption was artifact of the measurement systems, particularly the light source; however, for the range of interest (between absorption edges of GaAs and AlGaAs), stable response was obtained.

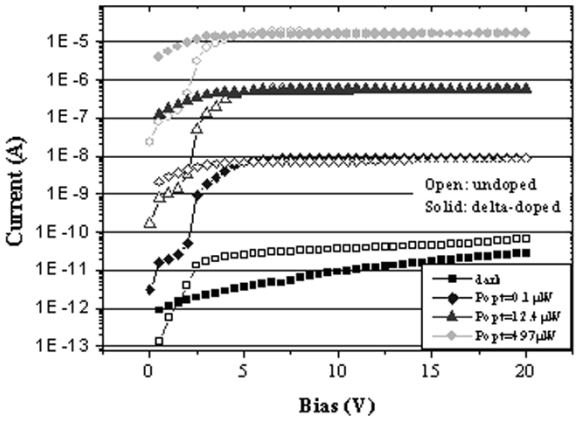

Fig. 9. Comparison of *I–V* behavior between the undoped device and delta-doped device with a resonant cavity.

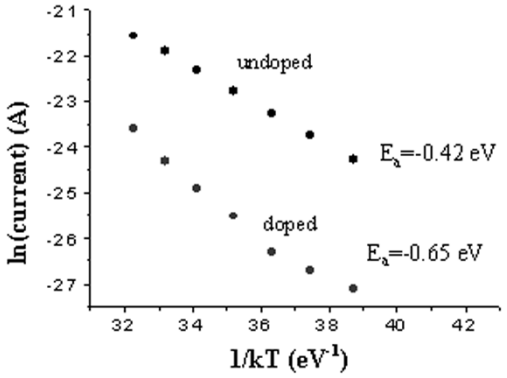

Fig. 10. Arrhenius plot for the undoped device and delta-doped RCE device at 10-V bias.

B. RCE–HMSM Static Characterization

Similar measurements were performed on the RCE-based devices; Fig. 9 shows *I–V* curves under dark and under dc light excitation at two different optical powers for the devices with and without delta doping. Under dark, the doped sample shows a soft increase of the current with voltage, with values, at 20 V, lower than 30 pA. The behavior of the undoped sample is rather different, as the current strongly increases at low voltage (2–3 V) up to approximately 30 pA. As the voltage is raised, current slowly increases up to almost 100 pA at the maximum voltage. It is worth noting that the lower values for current of the doped sample are in qualitative agreement with the effect of the repulsion between the electrons in the metal contact and the electrons in the 2-DEG (similar to the photodetectors with uniform doping) above. This is further evidenced in Fig. 10 where an Arrhenius plot compares dark current conduction for delta-doped and undoped samples at various temperatures. The diagram highlights a large difference of approximately 0.23 eV in activation energy at 10 V, which is calculated from the slope of the $\ln(I)$ versus $1/kT$ plot.

The dc light response was measured using a 850-nm pigtailed laser with the optical fiber of a 9-μm core positioned just in the proximity of, but not perpendicular to, the active area of the device. Due to the very low leakage current and to the good

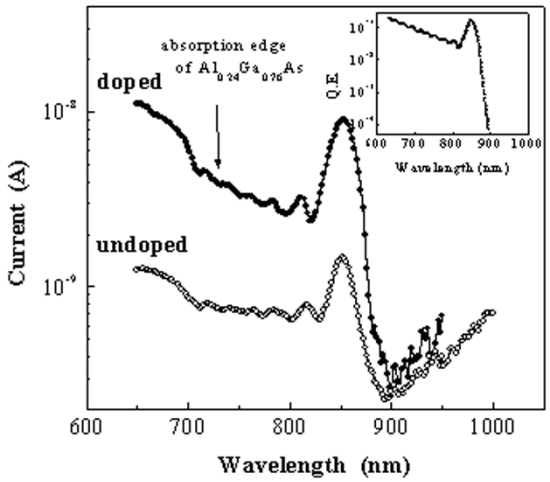

Fig. 11. Photocurrent spectral response for the undoped device and delta-doped device with a resonant cavity; inset shows the calculated quantum efficiency.

responsivity, both detectors show a large dynamic response, the undoped samples showing lower photocurrent values at low voltage. However, for $V > 2 - 3$ V, the photocurrent curves of both samples merge and strongly saturate. Saturation indicates complete collection of the photogenerated carriers.

Fig. 11 illustrates the experimental photocurrent spectral response of the doped and undoped RCE–HMSM photodetectors with 10-V bias. The resonant peak is around 850 nm and the FWHM value is 30 nm. An increase of photocurrent is observed around 710 nm, which is due to absorption in AlGaAs layers. We note that the spectral response is, at all the wavelengths, much higher for the doped than for the undoped device. Some photocurrent oscillations are evident between 720–850 nm in both devices, which can be attributed to the effect of the Bragg reflector. The inset shows results from simulation of the internal quantum efficiency, defined as the ratio of absorbed to incident photons, that show a clear resonant peak at 850 nm with 26-nm FWHM, which corroborates the experimental data. However, the inset indicates a gradually increasing shoulder on the high-energy side; this is probably due to overestimating the absorption of GaAs at high energies.

A quantitative comparison between current values of Figs. 11 and 9 is difficult due to variation of light intensity, especially at the low-output levels of a monochrometer; however, using a laser source at 850 nm, responsivity of 0.15 A/W for the doped versus 0.11 A/W for the undoped RCE–HMSM device was measured. The external quantum efficiencies are also calculated to be 21.3% and 16.7% for these cases, respectively. By the same standard, the external quantum efficiency of a thick, i.e., several micrometers, MSM photodetector with a 4-μm finger-spacing and a 2-μm finger-width geometry is 46.3%, calculated by accounting for reflection into the air, as well as reflection from metal surfaces. In our case, the thickness of the absorption layer is limited to 117 nm in order to balance the tradeoff between the quantum efficiency and speed. If resonant cavity were not considered, for such a thickness, the external quantum efficiency would be less than 4%, assuming an absorption coefficient of 0.75 μm^{-1} at 850 nm. Thus, the effect of the resonant cavity

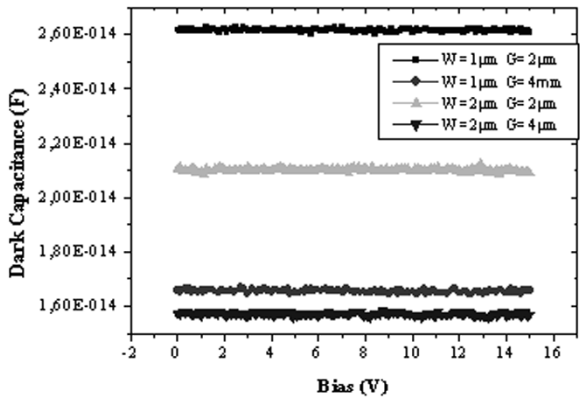

Fig. 12. *C–V* curves for four different interdigital structures of the RCE delta-doped devices.

TABLE I
MEASURED AND THEORETICAL GEOMETRIC CAPACITANCE VALUES

Interdigital Structure	Measured Capacitance (fF)	Calculated Capacitance (fF)
W=1μm G=2μm	26	27
W=1μm G=4μm	16.5	13
W=2μm G=2μm	21.5	26.5
W=2μm G=4μm	16	14

is apparent in the overall optical response, but cannot explain the differences observed for identical layer structures that only differ in doping of a couple of atomic layers. This indicates that the optical properties due to the layered structure are responsible for the shape of the spectral response; however, the magnitude difference can only be explained by the electronic properties of absorption, transport, and collection of carriers.

By using a precision LCR meter, we also performed capacitance measurements at 1-MHz frequency and 30-mV amplitude of the oscillating voltage as a function of a constant applied voltage on delta doped devices. The *C–V* curves of samples having different interdigital contact finger width (W) and inter-finger distance (G) are reported in Fig. 12. Interestingly, these samples show capacitance values independent of the applied voltage. We observe in Table I good agreement between the capacitance values measured at high voltages and those calculated based on geometric capacitance of the interdigital planar devices [16] as follows:

$$C \approx \frac{\pi \varepsilon_S A}{2(W+G)\log\left(2(1+\sqrt{K})/(1-\sqrt{K})\right)} \tag{3}$$

where ε_S is the GaAs permittivity, A is the active area, and $K = [1-\tan^4(\pi W/4(W+G))]^{1/2}$ is a dimensionless quantity.

IV. DYNAMIC CHARACTERIZATION

High-speed time measurements were performed using a mode-locked Ti sapphire laser, operating at a repetition rate of 76 MHz that generates 125-fs duration pulses. The wavelength of the tunable laser was at 850 nm; the average optical power was 0.1 mW, which corresponds to a pulse energy of approximately 1.4 pJ. The optical pulses impinge on the photodiodes biased through a bias tee. The photodiode RF signal is measured

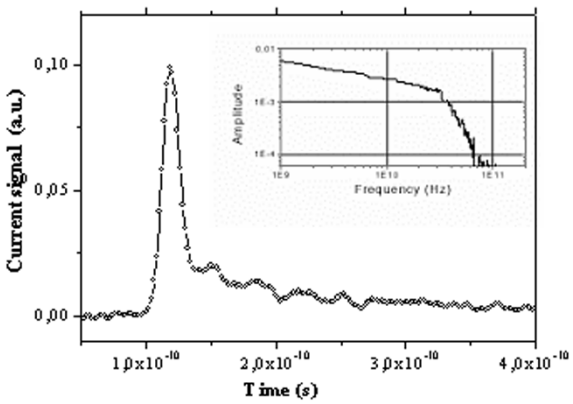

Fig. 13. Temporal response of a $W = 2\ \mu$m $G = 2\ \mu$m uniform doped device (long trace data); inset shows the frequency response.

TABLE II
COMPARISON OF TIME RESPONSE PEAK AMPLITUDE, PULSEWIDTH, AND CUTOFF FREQUENCY OF RESPONSE FROM SHORT TRACE DATA FOR DIFFERENT INTERDIGITAL STRUCTURES OF HMSM UNIFORMLY DOPED DEVICES, BIASED AT 10 V

Contact Width, Gap (μm)	Ampl. low-doped (a.u.)	Ampl. high-doped (a.u.)	Width low-doped (ps)	Width high-doped (ps)	Cut-off freq. low-doped (GHz)	Cut-off freq. high-doped (GHz)
1,2	0.218	0.239	8.682	7.739	26.9	30.5
2,2	0.262	0.364	8.790	7.744	29.3	33.0
1,4	0.185	0.216	8.226	7.311	34.2	24.4
2,4	0.157	0.218	9.259	8.153	28.1	31.7

on-wafer with a 50-GHz sampling oscilloscope at different acquisition times in order to evaluate the complete transport mechanism of the devices. Two sets of data were taken: one with a higher resolution, but a short duration of 50 ps, and the other with a long duration of 400 ps. The long trace data allows one to examine the behavior of slowly moving carriers, while the short trace shows high-speed dynamics of the device. No attempt was made to de-convolve the intrinsic response from the measured data, which includes the effects of test setup, as well as external circuitry. A large number of devices were tested; typical data is presented below.

A. HMSM Dynamic Characterization

Fig. 13 reports a typical long trace for a uniformly doped device with $W = 2\ \mu$m and $G = 2\ \mu$m, which shows a short (less than 10-ps long) peak with short FWHM that is followed by a typical long tail of low amplitude due to the effect of the slow-moving carriers, as well as the ringing of the tail that is attributed to the test setup. The inset of this figure also shows the fast Fourier transform (FFT) of the data indicating a sharp drop in amplitude after 30 GHz. Table II summarizes the results for the short trace acquisition time: for each contact geometry, the peak amplitude, pulsewidth calculated from a Gaussian fit of the data, and optical cutoff frequency, i.e., the frequency at which output current that is proportional to optical power reaches half its low frequency value, are reported.

The peak amplitude of the time response is seen to be consistently higher for the higher doped device compared to the lower

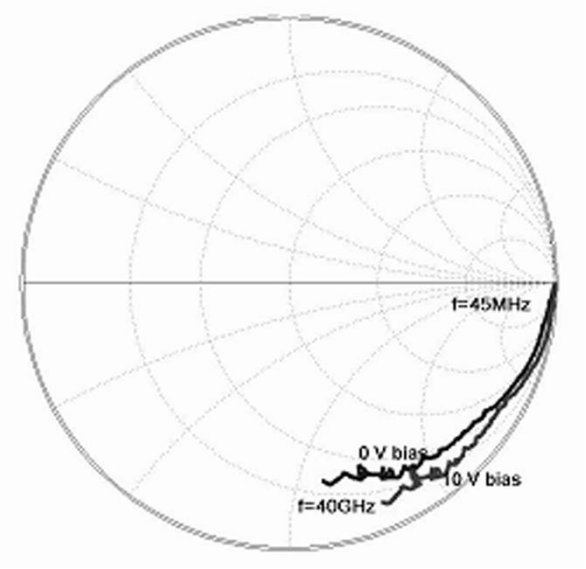

Fig. 14. Measured microwave reflection coefficients of a $W = 2\ \mu$m $G = 2\ \mu$m uniform doped device, for 0- and 10-V applied dc bias.

doped one. Importantly, the FWHM is also consistently shorter in the higher doped device indicating that increase in amplitude response is not at the cost of the decrease in speed response. The cutoff frequency also shows the same trend with the exception of the device with $W = 1$ and $G = 4$. The discrepancy is partially due to the fact that the frequency response is simply the FFT of the raw data. As mentioned above, data has not been de-convolved since it is seen that the values of FWHM, especially for the high doping device, are close to the limit of the test setup. Also, lack of scaling of the time response with lateral transit dimensions was observed, which is under investigation, hence, a qualitative conclusion regarding the observed higher speed of response for the higher doped device is currently sufficient; a higher resolution electrooptical sampling method is currently being conducted in order to more accurately describe dynamic device behavior.

Due to the lack of high-modulation frequency sources at 850-nm wavelength, microwave reflection coefficient (S_{11}) measurements were performed on-wafer in the frequency range of 45 MHz–40 GHz using a vector network analyzer. The S_{11} measurement shown in Fig. 14 illustrates a typical Smith chart, describing the impedance of a $W = 2\ \mu$m $G = 2\ \mu$m device (Z_{meas}). Assuming a known circuit topology for typical interdigital heterojunction structures [20], [21], a theoretical impedance $Z_{\text{circ}}(Rs, Rp, Cj, Cp, Ls)$ is derived. These components correspond to: 1) Cj being junction capacitance; 2) Rp being the parallel resistance; 3) Rs being the serial resistance; and 4) Cp and Ls being the contacts and leads capacitance and inductance, respectively. Using an optimization procedure, we have found the minimum of the five-variable function $Z_{\text{meas}} - Z_{\text{circ}}(Rs, Rp, Cj, Cp, Ls)$, thus fitting the components values for different interdigital geometries and different applied bias voltages in the frequency range of 45 MHz–40 GHz. The equivalent circuit is shown in Fig. 15. We have observed that the equivalent circuit reported is approximately the same at high frequencies $(f > 10$ GHz$)$

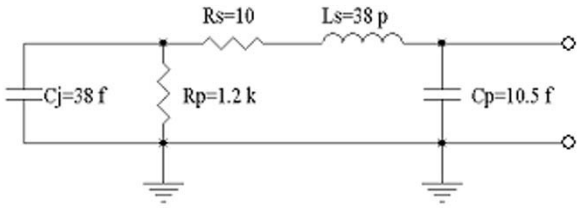

Fig. 15. Device equivalent circuit of a $W = 2\ \mu$m $G = 2\ \mu$m uniform doped device at 10-V applied dc bias.

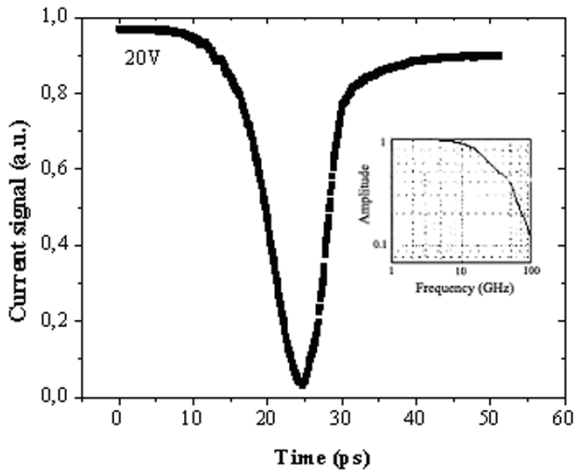

Fig. 16. Temporal response of a $W = 1\ \mu$m $G = 4\ \mu$m RCE delta-doped device (short trace data); inset shows the frequency response obtained from the Fourier transform.

at the operative 10-V bias voltage. Such an equivalent circuit is useful for the design of impedance-matched amplifier circuitry that is necessary for photoreceivers.

B. RCE–HMSM Dynamic Characterization

Fig. 16 shows the short trace temporal response of a delta-doped RCE–HMSM photodetector with geometry $W = 1\ \mu$m and $G = 4\ \mu$m measured at 20-V bias. From this figure, the FWHM of the time response is 8.1 ps, its rise time is 8.8 ps, and its fall time is 9 ps. The FFT of the data is shown in the inset of this figure and has a cutoff frequency of 34 GHz. The fact that the rise time, fall time, and FWHM of the peak are comparable suggests that the limits of the resolution of the measurement system are reached. A large number of devices of varying geometries, both delta-doped and undoped, were tested; typical results are presented in Table III for a bias of 20 V, where the frequency cutoff corresponds to the optical 3-dB point of the FFT of the time response.

The peak amplitude has been properly normalized to take into account the active area of the device. The results are consistent with the previous case, showing that the doped samples have peak amplitude always greater than the undoped samples. In Fig. 17, we report the peak amplitude of the induced pulses as a function of the applied voltage. The doped sample consistently shows a higher peak of response compared to the undoped one.

Time-response speed based on width values reported in Table III also shows that, with the exception of one device

TABLE III
COMPARISON OF PEAK AMPLITUDE, PULSEWIDTH, AND CUTOFF FREQUENCY OF RESPONSE (SHORT TRACE DATA) FOR DIFFERENT INTERDIGITAL STRUCTURES OF RCE–HMSM DELTA-DOPED AND UNDOPED DEVICES, BIASED AT 20 V

Contact Width, Gap (μm)	Ampl. delta doped (a.u.)	Ampl. un-doped (a.u.)	Width delta doped (ps)	Width un-doped (ps)	Cut-off freq. delta doped (GHz)	Cut-off freq. un-doped (GHz)
1,2	0.331	0.192	7.97	9.45	44.0	26.9
2,2	0.292	0.207	11.9	10.38	25.6	25.6
1,4	0.252	0.103	7.03	10.16	34.2	29.3
2,4	0.206	0.111	7.11	12.04	26.3	24.4

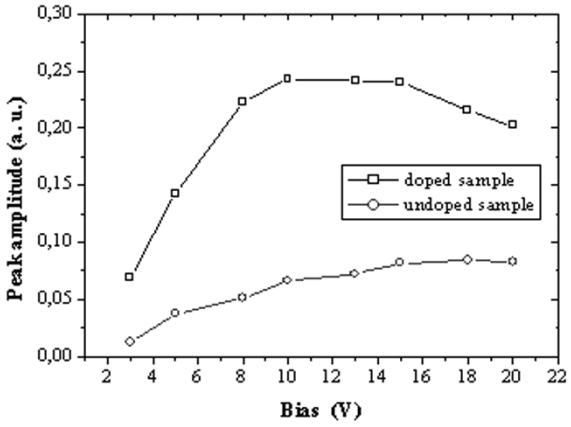

Fig. 17. Peak amplitudes of time response as a function of the applied voltage for the RCE delta-doped and undoped devices with $W = 1\ \mu$m and $G = 4\ \mu$m.

($W = 2$, $G = 2$), doped samples have a faster response compared to the undoped ones. Furthermore, the samples with $G = 2\ \mu$m have peak amplitude always greater than those with $G = 4\ \mu$m, which is indicative of an incomplete collection of charge, probably due to trapping processes and change of transit path in the doped device. Again, no attempt was made to extract the intrinsic response of the detectors from the measurements since results were close to the limit of the resolution of the test setup. Devices with embedded transmission lines suitable for the higher resolution electrooptic sampling measurement techniques have been fabricated in order to investigate the dynamic behavior. It is quite interesting that the photodetector with higher responsivity also have higher speed, but canonical quantum efficiency-bandwidth product limitation only applies to structures where depleted absorption layers lead to such tradeoffs. In the RCE–HMSM device, proper engineering of the internal field profile and optical properties allows a more efficient collection of optically generated electrons leading to simultaneous improvement of efficiency and time response.

V. CONCLUSION

We have reported on a comprehensive experimental study of four photodetector devices that have the benefit of compatibility with established HEMT technology and are, thus, more conducive to monolithic integration with high-speed OEIC. These heterojunction-based planar devices all use the wide-gap material to enhance the Schottky barrier height between the metal and semiconductor. We have shown that doping of this layer produces an internal electric field that aids in the transport and collection of photoelectrons. First, devices were compared when the only variant was the doping level, thus showing the effect of this internal aiding field. Current–voltage data shows the low dark current and high dynamic range of the device. Current–temperature data indicate that the activation energy, a measure proportional to the barrier height, increases for the high doping device. This is unexpected if interpreted on the basis of the effect of doping on Schottky barrier lowering, but is consistent with our previous formulation of the repulsion of the thermionically emitted carriers by the electron cloud of the 2-DEG. Photocurrent spectra comparing the two devices show a marked increase at all wavelengths for the high doped device. In addition, we have characterized an RCE–HMSM photodetector, demonstrating the performance improvement due to a resonant-cavity produced by adding a DBR to a properly chosen absorption layer thickness. Two variants of this device are also compared where a delta-doping layer is added to the top wide-gap layer. Presence of this delta-doped sheet plays an important role in terms of barrier enhancement and internal electric field aiding in the transport of photocarriers. Thus, these devices exhibit very low dark current and capacitance, wavelength selectivity, and sensitivity. High-speed time-response data indicates that the devices easily operate in tens of gigahertz with the doped devices showing a much higher peak of response with no adverse effect, even a slight improvement, of FWHM. Finally, on-wafer frequency-domain measurements with a network analyzer were performed, which allowed the derivation of an RF small-signal model that is necessary for designing complete photoreceivers for optical communication applications. We suggest that these HMSM devices are photodetectors suitable for "general-purpose" opto-electronic applications such as remote sensing, light detection and ranging (LIDAR), and medical imaging, while the RCE devices are perhaps better for local-area, fiber-optic, and short-haul free-space telecommunication applications.

ACKNOWLEDGMENT

The authors gratefully acknowledge the time-response measurements performed by Dr. M. Currie, Naval Research Laboratory (NRL), Washington, DC.

REFERENCES

[1] P. Fay, C. Caneau, and I. Adesida, "High-speed MSM/HEMT and p-i-n/HEMT monolithic photoreceivers," *IEEE Trans. Microwave Theory Tech.*, vol. 50, pp. 62–67, Jan. 2002.
[2] J. C. Campbell, H. Nie, C. Lenox, G. Kinsey, P. Yuan, A. L. Holmes, and B. G. Streetman, "High-speed, low-noise avalanche photodiodes," in *Optical Fiber Communication Conf.*, vol. 4, 2002, pp. 114–116.
[3] M. Lang, W. Bronner, W. Benz, M. Ludwig, V. Hurm, G. Kaufel, A. Leuther, J. Rosenzweig, and M. Schlechtweg, "Complete monolithic integrated 2.5 Gbit/s optoelectronic receiver with large area MSM photodiode for 850 nm wavelength," *Electron. Lett.*, vol. 37, pp. 1247–1249, Sept. 2001.
[4] C. C. Ku, C. H. Lin, M. H. Tsai, J. T. Ting, and R. H. Yuang, "A 1.25 Gb/s GaAs OEIC for gigabit Ethernet," in *IEEE GaAs IC Symp.*, 1999, pp. 95–98.

[5] X. J. Li, J. P. Ao, R. Wang, W. J. Liu, Z. G. Wang, Q. M. Zeng, S. Y. Liu, and C. G. Liang, "An 850 nm wavelength monolithic integrated photoreceiver with a single-power-supplied transimpedance amplifier based on GaAs PHEMT technology," in *IEEE GaAs Dig.*, 2001, pp. 65–69.
[6] J. H. Burroughes, "H-MESFET compatible GaAs/AlGaAs MSM photodetector," *IEEE Photon. Technol. Lett.*, vol. 3, pp. 660–662, July 1991.
[7] J. W. Seo, A. A. Ketterson, D. G. Ballegeer, K. Y. Cheng, I. Adesida, X. Li, and T. Gessert, "A comparative study of metal–semiconductor–metal photodetectors on GaAs with indium–tin–oxide and Ti/Au electrodes," *IEEE Photon. Technol. Lett.*, vol. 4, pp. 888–890, Aug. 1992.
[8] J. S. Wang, C. G. Shih, W. H. Chang, J. R. Middleton, P. J. Apostolakis, and M. Feng, "11 GHz bandwidth optical integrated receivers using GaAs MESFET and MSM technology," *IEEE Photon. Technol. Lett.*, vol. 5, pp. 316–318, Mar. 1993.
[9] M. Bitter, R. Becht, W. Hunziker, and H. Melchior, "Molithically integrated 40-Gb/s InP/InGaAs PIN/HBT optical receiver module," in *11th Int. Indium Phosphide and Related Materials Conf.*, May 1999, pp. 381–384.
[10] M. Kyomasu, "Development of an integrated high speed silicon PIN photodiode sensor," *IEEE Trans. Electron. Devices*, vol. 42, pp. 1093–1099, June 1995.
[11] B. Nabet, "A heterojunction metal–semiconductor–metal photodetector," *IEEE Photon. Technol. Lett.*, vol. 9, pp. 223–225, Feb. 1997.
[12] A. Anwar and B. Nabet, "Barrier enhancement mechanisms in heterodimensional contacts and their effect of current transport," *IEEE Trans. Microwave Theory Tech.*, vol. 50, pp. 68–71, Jan. 2002.
[13] S. M. Sze, *Physics of Semiconductor Devices*, 2nd ed. New York: Wiley, 1981.
[14] B. Nabet, A. Cola, F. Quaranta, M. Cesareo, R. Rossi, R. Fucci, and A. Anwar, "Electron cloud effect on current injection across a Schottky contact," *Appl. Phys. Lett.*, vol. 77, no. 24, pp. 4007–4009, Dec. 2001.
[15] M. S. Unlu and S. Strite, "Resonant cavity enhanced photonic devices," *J. Appl. Phys.*, vol. 78, no. 2, pp. 607–639, July 1995.
[16] J. B. D. Soole and H. Schumacher, "Transit-time limited frequency response of InGaAs MSM photodetectors," *IEEE Trans. Electron Devices*, vol. 37, pp. 2285–2291, Nov. 1990.
[17] M. Horstmann, K. Schimpf, M. Marso, A. Fox, and P. Kordos, "16 GHz bandwidth MSM photodetector and 45/85 GHz $f_T/f_{\max}$ HEMT prepared on an identical InGaAs/InP layer structure," *Electron. Lett.*, vol. 32, no. 8, pp. 763–764, Apr. 1996.
[18] S. Adachi, "GaAs, AlAs, and $A1_XGa_{1-X}As$: Material parameters for use in research and device applications," *J. Appl. Phys.*, vol. 58, no. 3, pp. R1–R29, Aug. 1985.
[19] X. Chen, B. Nabet, F. Quaranta, A. Cola, and M. Currie, "A resonant-cavity-enhanced heterostructure metal–semiconductor–metal photodetector," *Appl. Phys. Lett.*, vol. 80, no. 17, p. 3222, Apr. 2002.
[20] M. Tomaska, F. Uherek, and J. Jakabovic, "High-speed heterostructure photodetectors characterization," in *2nd Int. Advanced Semiconductor Devices and Microsystems Conf.*, Oct. 1998, pp. 99–102.
[21] M. Tomaska, M. Marso, A. Fox, and P. Kordos, "Microwave properties of the MSM photodetectors with 2-DEG," in *2nd Int. Advanced Semiconductor Devices and Microsystems Conf.*, Oct. 1998, pp. 295–298.

Bahram Nabet (M'89) received the B.S.E.E. degree (with honors) from Purdue University, West Lafayette, IN, in 1977, and the M.S.E.E. and Ph.D. degrees from the University of Washington, Seattle, in 1985 and 1989, respectively.

In 1989, he joined the faculty of Drexel University, Philadelphia, PA, where he is currently a Professor of electrical and computer engineering and Associate Dean for Special Projects with the College of Engineering. He coauthored two books and over 90 refereed publications. His areas of research include semiconductor devices, opto-electronics, reduced dimensional systems, and fiber-optic networks and devices. He has been a Senior Visiting Scientist in Brazil and Italy and was on sabbatical leave with Telcordia Applied Research Inc.

Dr. Nabet is a member of the American Association for the Advancement of Science (AAAS), the American Association for Higher Education (AAHE), and Eta Kappa Nu. He was the recipient of six Best Professor Teaching Awards presented by students, as well as a departmental and a university-wide teaching award.

Adriano Cola was born in La Spezia, Italy, in 1961. He received the Lode Honor degree from the University of Bari, Bari, Italy, in 1986, and the Ph.D. degree in physics from the University of Bari, Bari, Italy, in 1991.

In 1992, he joined the Material Science Department, Lecce University, Lecce, Italy. He spent one year involved with post-doctoral studies with the Centre National de la Recherche Scientifique (CNRS)–Laboratoire d'Etudes des Propriétés Electroniques des Solides (LEPES), Grenoble, France, and at the National Institute of Nuclear Physics, Pisa, Italy. In 1994, he joined the Institute of New Materials for Electronics (IMM), Consiglio Nazionale delle Ricerche (CNR), Lecce, Italy, becoming a permanent staff member in 1998 and a Senior Researcher in 2001. His main research interests are the transport properties of semiconductor material and devices. Beginning with the investigation of Schottky barriers, he has been involved in leading research projects on GaAs and CdTe X-ray detectors for applications in medicine radiology and astronomy. Recently, in collaboration with Drexel University, Philadelphia, PA, where he spent the 2001 fall term as a Visiting Professor, he contributed to the development of photodetectors of new conception that take advantage of reduced dimensionality quantum regimes in order to improve their performance in terms of speed and sensitivity. He has coauthored over 60 refereed journal papers and 40 conference publications.

Andrea Cataldo was born in Galatina, Lecce, Italy, in November 1972. He received the Materials Engineering degree from the University of Lecce, Lecce, Italy, in 1998, and is currently working toward the Ph.D. degree at the University of Lecce.

His main research interests are in the field of electronic measurements. He is also involved in research activities that include characterization and simulation of semiconductor devices, opto-electronics, microwave measurements, and modeling.

Xiying Chen received the B.Sc. degree in applied physics and M.Sc. degree in condensed matter physics from Fudan University, Shanghai, China, in 1993 and 1996, respectively, and the Ph.D. degree from Drexel University, Philadelphia, PA, in 2002.

From 1993 to 1996, she was with the Applied Surface Physics National Key Laboratory, Fudan University, where she was involved with the growing sulfur passivation layer on GaAs surfaces by using vapor deposition, microwave glow discharge, and high-voltage glow discharge, and characterizing the optical and electronic properties of passivation layers on GaAs surfaces. From 1998 to 2002, she was with the Optoelectronic Device Group, Drexel University, where her research concerned designing InP- and GaAs-based opto-electronic devices for optical communication and characterizing static and dynamic device behavior. In 2002, she was with the Center for Microwave/Lightwave Laboratory, Drexel University, where she was involved in the design and building of microchip lasers for high-speed communications. She is currently involved in developing Flash memory devices with the Mosel Vitelic Corporation, San Jose, CA.

Fabio Quaranta, photograph and biography not available at time of publication.